Proceedings of ASME Turbo Expo 2020
Turbomachinery Technical Conference and Exposition
GT2020
June 22-26, 2020, London, England

GT2020-15229

EFFECTS OF AXIAL CASING GROOVES ON THE STRUCTURE OF TURBULENCE IN THE TIP REGION OF AN AXIAL TURBOMACHINE ROTOR

Huang Chen[1], Yuanchao Li[1], Subhra Shankha Koley[1], Joseph Katz [1*]

[1] Johns Hopkins University, Department of Mechanical Engineering, Baltimore, MD, USA
*katz@jhu.edu

ABSTRACT

Challenges in predicting the turbulence in the tip region of turbomachines include anisotropy, inhomogeneity, and non-equilibrium conditions, resulting in poor correlations between the Reynold stresses and the corresponding mean strain rate components. The geometric complexity introduced by casing grooves exacerbates this problem. Taking advantage of a large database collected in the refractive index-matched liquid facility at JHU, this paper examines the evolution of turbulence in the tip region of an axial turbomachine with and without axial casing grooves, and for two flow rates. The semi-circular axial grooves are skewed by 45° in the positive circumferential direction, similar to that described in Müller et al. [1]. Comparison to results obtained for an untreated endwall includes differences in the distributions of turbulent kinetic energy (TKE), Reynolds stresses, anisotropy tensor, and dominant terms in the TKE production rate. The evolution of TKE at high flow rates for blade sections located downstream of the grooves is also investigated. Common features include: with or without casing grooves, the TKE is high near the tip leakage vortex (TLV) center, and in the shear layer connecting it to the blade suction side tip corner. The turbulence is highly anisotropic and inhomogeneous, with the anisotropy tensor demonstrating shifts from one dimensional (1D) to 2D and to 3D structures over small distances. Furthermore, the correlation between the mean strain rate and Reynolds stress tensor components is poor. With the grooves, the flow structure, hence the distribution of Reynolds stresses, becomes much more complex. Turbulence is also high in the corner vortex that develops at the entrance to the grooves and in the flow jetting out of the grooves into the passage. Consistent with trends of production rates of normal Reynolds stress components, the grooves increase the axial and reduce the radial velocity fluctuations compared to the untreated endwall. These findings introduce new insight that might assist the future development of Reynolds stress models suitable for tip flows.

Keywords: Turbulence, Reynold stresses, casing treatment, compressor stall, CFD

NOMENCLATURE

A	through flow area
c	rotor blade tip chord
h	width of the rotor blade tip gap
H	rotor blade span
k	turbulence kinetic energy
L	nominal distance from the hub to the inner casing endwall
p_{exit}	static pressure at stator outlet
p_{in}	static pressure at IGV inlet
P	production rate of TKE, production rate of Reynolds stress
r, z, θ	radial, axial and circumferential coordinates
r^*	normalized radial coordinate
s	rotor blade chordwise coordinate
S_{ij}	mean strain rate tensor
T	motor input torque
u_r, u_z, u_θ	radial, axial and circumferential velocity
U_T	rotor blade tip speed
u'	velocity fluctuation
V_z	averaged axial velocity in the rotor passage
ν_T	eddy viscosity
ρ	NaI solution density
φ	flow coefficient
ψ_{SS}	static-to-static pressure rise coefficient
ω	vorticity
Ω	rotor angular velocity
$< >$	ensemble-averaged quantity

ABBREVIATIONS

ACG	Axial Casing Groove
CFD	Computational Fluid Dynamics
JHU	Johns Hopkins University

NASA	National Aeronautics and Space Administration
PS	Pressure Side
LES	Large-Eddy Simulation
RANS	Reynolds-Averaged Navier-Stokes
SPIV	Stereoscopic Particle Image Velocimetry
SS	Suction Side
TKE	Turbulent Kinetic Energy
TLV	Tip Leakage Vortex

INTRODUCTION

Computational fluid dynamics (CFD) is being widely used to simulate the flow in turbomachines [1–4]. Reynolds-averaged Navier-Stokes (RANS) simulations with different closure models for the Reynolds stresses are the most popular due to the low computational cost. Questions arise on the applicability of common Reynolds stress models for applications of RANS in turbomachines, which is inherently complicated with varying flow structure scales, and fast-changing strain rate fields. Issues associated with RANS turbulence models such as the generation of negative normal stresses [5], stagnation point anomaly [6], and anisotropy of turbulence [7,8] have been discussed extensively in previous publications. A comparison between different models [9] has shown that using full Reynolds stress transport models could improve the results by introducing anisotropy to the simulation. Large-eddy simulation (LES) provides a better prediction of turbulence in turbomachines, but its applicability limited at the present time by high computational cost and issues associated with modeling the sub-grid stresses. Hence, currently, RANS simulation supported by calibrations of models by experimental data [10,11] is still the first choice for practical applications. Further advances in the development of turbulence models require high-resolution experimental data, which is challenging in the complex environment of turbomachines. Our past studies in the refractive index matched facility at JHU using stereoscopic-PIV (SPIV) have examined the flow and turbulence in the tip region of turbomachines in great detail [12–14], and have addressed a series of issues in modeling them [15,16]. The prevailing non-equilibrium condition in the tip region has challenged the popular eddy-viscosity based turbulence models, which assumes isotropy of turbulence.

The applications of casing treatments to delay the onset of stall in turbomachines [17–23] further complicate the situation, introducing more challenges for popular turbulence models. The increased flow complexity involves the interaction of the tip flow with the groove, the re-orientation of the tip leakage vortex (TLV), and secondary flow structures generated by these interactions. Out past studies have examined the dynamics of the fluid-groove interactions for skewed semicircular casing grooves [24] (ACGs) at different flow rates [25,26]. Results have shown that when the blade is passing the groove, part of the TLV and the circulation carried with it is entrained into the groove at a low flow rate. Flow separation at the groove corner generates a corner vortex rotating in the opposite direction of the TLV. At a high flow rate, the TLV entrains the corner vortex into the main passage, contributing to blockage effects. The reinjected flow from upstream of the groove enhances the mixing and generates a layer with elevated turbulence.

In this study, we utilize the data set for the flow within and around an axial casing groove to examine the spatial distributions of turbulent kinetic energy, individual Reynolds stress components, and associated dominant TKE production terms at two different flow rates. The results are compared with data obtained for the same machine with a smooth endwall. This comparison reveals several differences, such as a shift of the dominant Reynolds normal stress term from the radial direction for the smooth endwall to the axial direction. This change is caused by axial contraction of the mean flow when the leakage flow enters the groove. Sample eddy viscosity distributions calculated from individual Reynolds stress and corresponding averaged strain-rate components show spatial variations from negative to large positive numbers, confirming that assumptions of isotropy and eddy viscosity-based Reynold stress models are inherently flawed. Furthermore, anisotropy maps show the structure of turbulence varies spatially from one dominant direction (1D) to 2D and to 3D over small distances. Yet, in spite of the differences, the spatial distributions of anisotropy also show some similar trends for different flow rates, with or without grooves. This observation opens possibilities to exploit the anisotropy structure for the development of data-driven models.

EXPERIMENTAL SETUP

Detailed descriptions of the JHU refractive index matched facility and the axial casing grooves can be found in [15,27,28] and in [25,26], respectively. Relevant geometric parameters for the compressor model and for the grooves are included in Table 1. The blades of the one and half stage compressor model, which is illustrated in Fig.1a, are based on the Low-Speed Axial Compressor facility at NASA Glenn Research Center. The rotor blades and casing are made of transparent acrylic, whose refractive index matches that of the working fluid, a concentrated aqueous solution of NaI. The resulting unobstructed optical access allows the implementations of optical measurement techniques. The semicircular axial casing grooves, with diameters of 65% of the blade axial chord, are located around the rotor leading edge, with 33% of the groove overlapping with the rotor, and the rest, extending upstream of the rotor (Fig.1b). The groove geometry is based on the numerical study described in Müller et al. [1]. The evenly spaced, four-per-passage grooves are skewed by 45° in the direction of rotor rotation (Fig.1c). SPIV has been used to quantify the flow field in meridional and radial planes, but only the former is discussed in this paper.

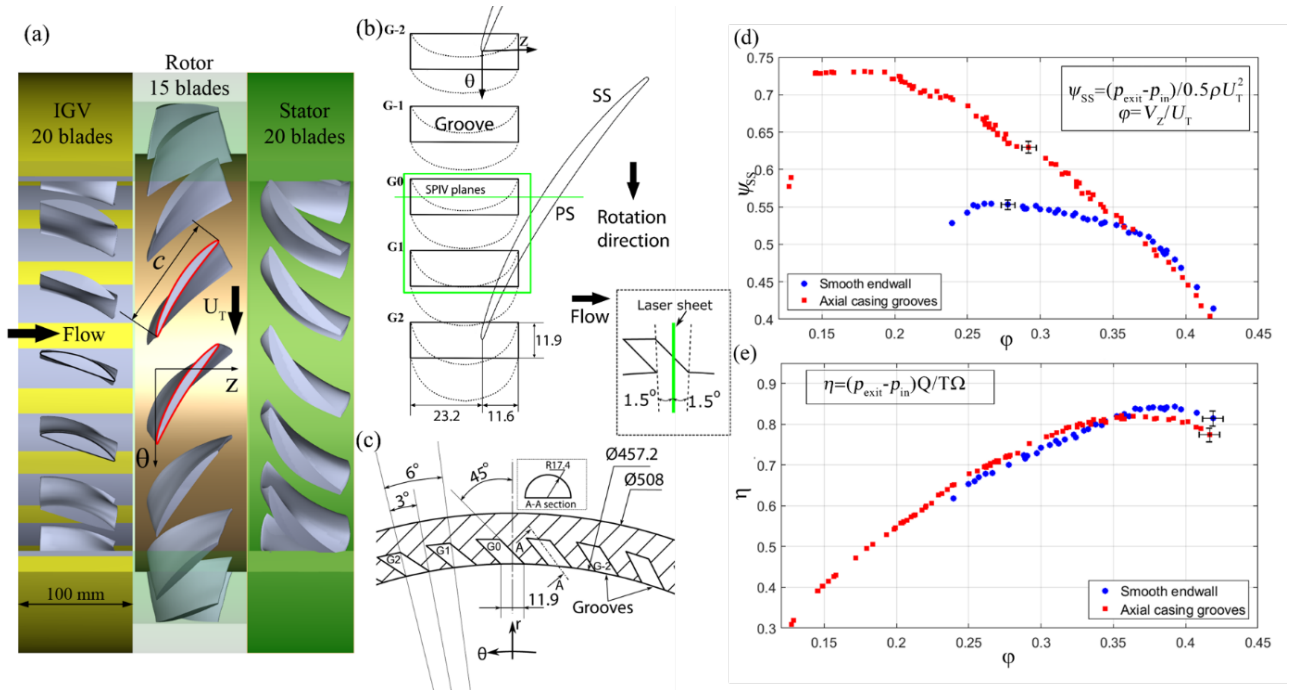

Figure 1: (a) Configuration of the one and a half stages compressor. (b, c) The semi-circular ACG configuration. (d, e) Performance and efficiency curves with and without the axial casing grooves

The optical setup, as well as calibration and data processing procedures for measuring the velocity distributions for the smooth and grooved endwalls are discussed in detail in [28] and [25,26], respectively. Briefly, two inclined cameras located on both sides of the meridional laser sheet are used to record the particle field images. The field of view for the smooth endwall is smaller than that for the ACG case owing to differences in the camera resolution used, and our interest to cover the entire range of the ACG in a single frame. However, the vector spacings are kept similar, namely 0.16mm for the smooth endwall and 0.14mm for the ACG. In addition, for the ACG case at high flow rates, the experiments have been conducted at two different axial locations, covering the tip flow from the upstream corner of the ACG up to 80% of the blade chord. By changing the delay between a shaft encoder connected to the rotor and the imaging system, the SPIV data has been obtained in a series of meridional planes covering an entire rotor passage. A chordwise coordinate system, s, which aligns with the rotor blade tip chord, is used to label the location of the sample planes. When s is normalized by the blade tip chord c, the rotor blade leading edge is located at s/c=0 and the trailing edge is at s/c=1. For the ACG data presented in this paper, the laser sheet cuts through the center of one of the grooves, as shown in the insert in Fig.1b. Additional mean flow data for other meridional planes cutting through this groove are presented in [25,26]. In each plane, flow condition, and blade orientation relative to the groove, 2500 statistically independent instantaneous samples are recorded to ensure the convergence of the turbulence statistics. Base on previous analysis [29], the uncertainty for the instantaneous velocity measurement is around 0.1 pixel when there are more than five particles in each interrogation window, corresponding to 0.4–0.8% of the tip speed. Because of the large number of samples, the uncertainty for ensemble-averaged values is at least an order of magnitude smaller. The data is presented in a cylindrical coordinate system (r, θ, z) whose origin is located at the center of the machine and coincides with the leading-edge plane. The corresponding velocity components are u_z, u_r, and u_θ. The ensemble-averaged velocity components for a specific blade orientation are denoted as U_i and the corresponding velocity fluctuations are calculated from $u_i'=u_i-U_i$. The ensemble-averaged Reynolds stress parameters denoted as $\langle u_i'u_j'\rangle$, and the turbulent kinetic energy, $k=0.5(\langle u_z'u_z'\rangle+\langle u_r'u_r'\rangle+\langle u_\theta'u_\theta'\rangle)$, are normalized by the blade tip speed, e.g., $k^*=k/U_T^2$.

Previously published performance and efficiency curves are shown in Figs.1d&e, respectively. The measurement procedures are discussed in detail in [15,26]. The flow coefficient φ is defined by $\varphi=V_Z/U_T$, where is V_Z is the spatially averaged axial velocity in the rotor passage (flow rate divided by the throughflow area). The static-to-static head rise coefficient is defined as $\psi_{SS}=(P_{exit}-P_{in})/0.5\rho U_T^2$, where $P_{exit}-P_{in}$ represents the pressure rise across the entire machine. The efficiency of the machine is calculated from $\eta=(P_{exit}-P_{in})Q/T\Omega$, where Q is the volumetric flow rate and T is the input torque measured at the shaft. As is evident, without casing grooves, the machine stalls at around φ=0.25. In contrast, the stall flow rate is reduced by 40%, to about φ=0.14, when the casing grooves are installed. However, at high flow rates, namely φ>0.35, the ACGs cause a slight decrease in head rise accompanied by a 2.8% loss of peak efficiency. Most of the data and discussions in this paper focused on the Reynolds stresses at φ=0.25 and φ=0.35, the former

corresponding to pre-stall flow rate of the smooth endwall, and the latter representing conditions near the best efficiency point of the machine.

RESULTS AND DISCUSSION

The discussion begins with a brief review of the tip flow-groove interactions at two different flow rates (Figs.2a&c), and a comparison to the tip flow structure of the smooth endwall case (Figs.2b&d). Detailed analyses for the smooth end wall can be found in [14,15,27,28], and the $\langle u_i'u_j' \rangle$ results for the machine with ACGs are presented in [25] for φ=0.25 and in [26] for φ=0.35. In the selected sample blade phase (s/c=0.44), the blade suction side (SS) just clears the downstream end of the groove. At φ=0.25 (Figs.2a&b), both the smooth and treated endwall flows feature a tip leakage flow, a tip leakage vortex (TLV), and a shear layer connecting the TLV to the suction side (SS) tip corner. However, a secondary corner vortex with an opposite vorticity sign forms at the downstream corner of the groove, owing to flow separation as the leakage flow enters the groove. As discussed in [25], suction of the tip flow into the groove and the resulting reduction in the TLV strength is one of the main causes for stall suppression by the casing groove. The entrained fluid then circulates around and is reinjected into the main passage flow at the upstream end of the groove. This reinjected flow generates a radially-oriented shear layer with negative vorticity at the upstream corner and a horizontal shear layer with

Table 1: Stage relevant geometrical parameters

Casing diameter (D) (mm)	457.2
Hub radius (r_{hub}) (mm)	182.9
Rotor passage height (L) (mm)	45.7
Rotor diameter (D_R) (mm)	453.6
Rotor blade tip chord (c) (mm)	102.6
Rotor blade span (H) (mm)	43.9
Rotor blade stagger angle (γ) (deg)	58.6
Rotor blade axial chord (c_A) (mm)	53.5
Measured tip clearance (h) (mm)	1.8 (0.0175c or 0.041H)
Axial casing groove diameter (mm)	34.8
Groove skew angle (deg)	45
Total number of grooves	60
Shaft speed (Ω) (rad s^{-1}) {RPM}	50.27 {480}
Rotor blade tip speed (U_T) (m s^{-1})	11.47
Reynolds number ($U_T c / \nu$)	1.07×10^6

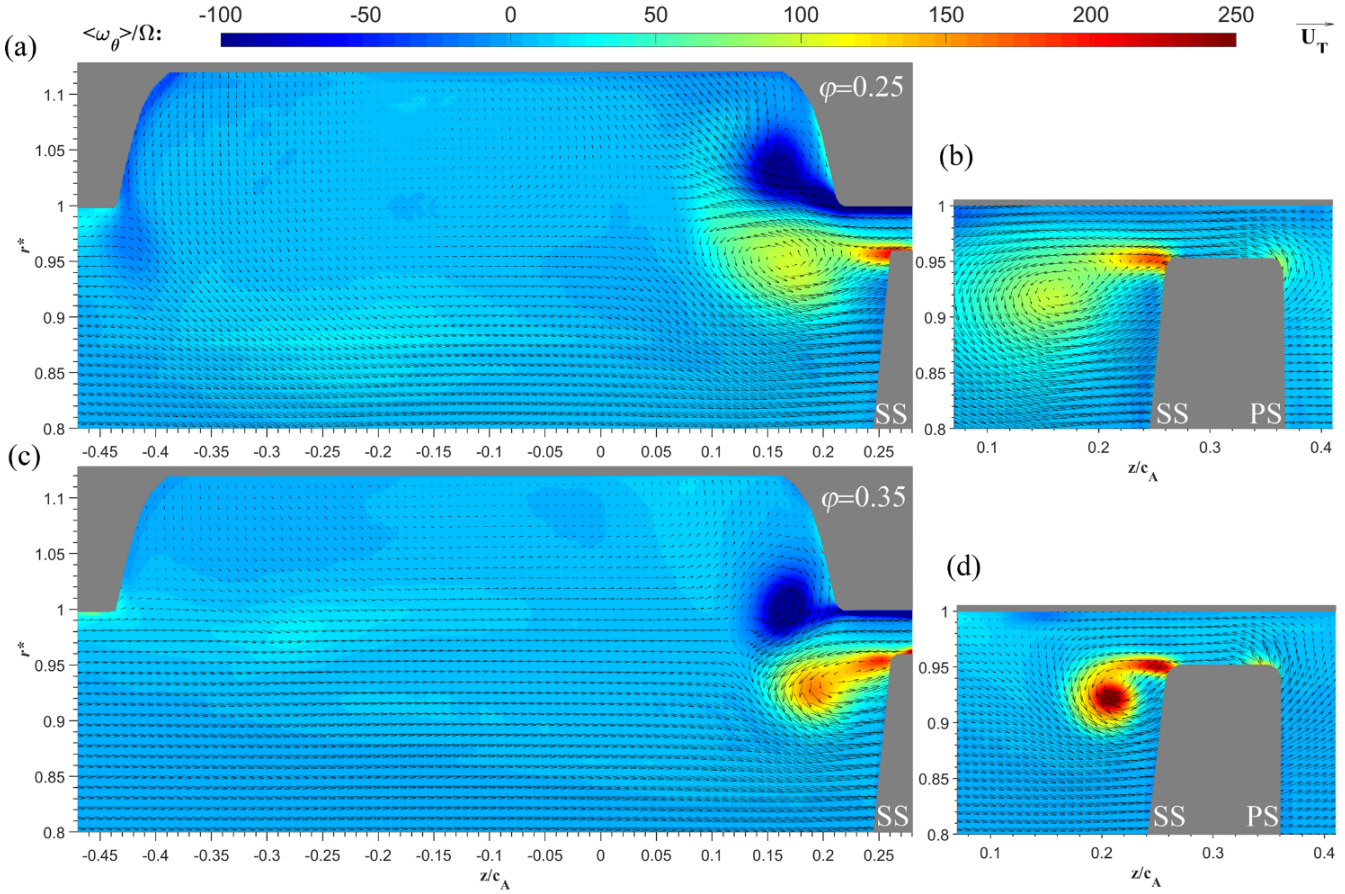

Figure 2: Ensemble-averaged circumferential vorticity distributions superimposed on the in-plane velocity vectors at s/c=0.44: (a, c) with, and (b, d) without casing grooves. The corresponding flow coefficients are: (a, b) φ=0.25, and (c, d) φ=0.35. The color scale and reference vector showing U_T apply to all cases. Vectors are diluted by 3:1 in both directions for clarity.

positive vorticity at the transition between the groove and main passage flow. This injection also causes periodic changes to the flow angle near the blade leading edge, which is another likely contributor to the delay of stall [25]. The TLV, corner vortex, and a horizontal shear layer with positive vorticity at the transition between the (much slower) reinjected fluid and the main passage flow can also be seen at φ=0.35 (Fig.2c). However, in this case, the corner vortex and some of the fluid associated with it are entrained into the main passage by the TLV at the downstream side of the groove. As shown later, this phenomenon contributes significantly to the turbulence production rate at high flow rates. Owing to these interactions, the peak vorticity in the TLV center is much lower for the grooved case compared with that of the smooth endwall (Fig.2d). In contrast, in spite of the effect of TLV suction into the groove at low flow rate, the peak vorticity and the TLV circulation of the grooved endwall are still higher than those of the smooth endwall (Figs.2a&b). This trend is caused by a shift in blade loading towards the leading edge, which increases the TLV strength of the grooved endwall at low *s*/*c*. However, as shown in [25], entrainment of the TLV into the groove decreases the TLV circulation rapidly further along the blade.

Turbulent kinetic energy distribution

Figure 3 compares the turbulence kinetic energy at φ=0.25 for three different blade orientations. In Figs3a&b the laser sheet cuts the blade at *s*/*c*=0.33 when the blade tip is partially overlapped with the downstream corner of the groove. Prominent TKE peaks can be identified at the centers of the TLV and the corner vortex as well as in the high shear region between them (Fig.3a). The reinjected flow exiting from the groove at the upstream end of the groove also generates a layer of elevated turbulence, but its strength is still one order of magnitude lower than the peaks appearing in the downstream corner. As the outflow with elevated turbulence interacts with the flow induced by the tip and corner vortices, it creates a broad turbulent region that surrounds these vortices. In comparison, near the smooth endwall (Fig.3b), the turbulence is high in the vortex center and in the shear layer connecting it to the SS tip corner. Furthermore, the TKE level on the pressure side (PS) of the blade is high over a broad area owing to the presence of remnant of a previous TLV and related unsteady secondary structures, including the backflow vortices [25]. This elevated turbulence propagates through the tip gap to the SS of the blade and is entrained into the flow surrounding the TLV. Because of this entrainment under pre-stall conditions of the smooth endwall, the TKE in the vicinity of the TLV is significantly higher than that observed at a high flow rate (Fig.4a). Such turbulent remnants of a previous TLV do not exist in the PS of the grooved endwall (Fig.3a), presumably since large fractions of the TLV are entrained into the ACGs, as discussed before.

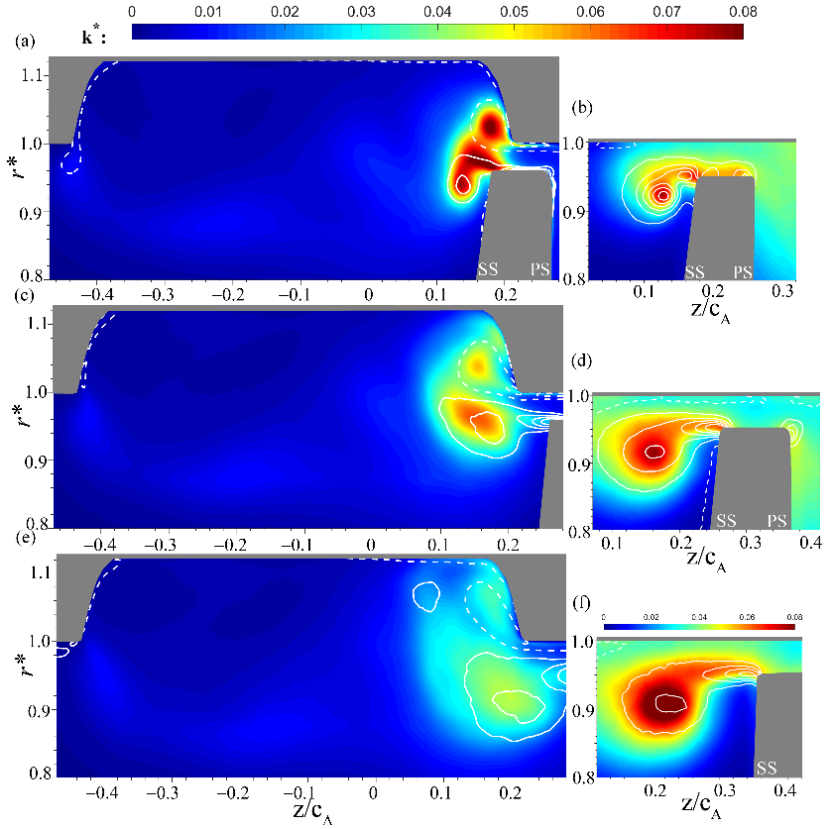

Figure 3: Evolution of turbulent kinetic energy for grooved and smooth endwalls at φ=0.25. Left column: with casing grooves; right column: smooth endwall. (a, b) *s*/*c*=0.33, (c, d) *s*/*c*=0.44, and (e, f) *s*/*c*=0.55. The white contour lines show the circumferential vorticity, with solid lines indicating $\langle\omega_\theta\rangle > 0$ and dashed lines $\langle\omega_\theta\rangle < 0$

At s/c=0.44, the blade is located just downstream of the groove (Fig.3c). The TKE peaks in the vortex centers and the shear layer are lower than those in the previous phase, but the region with elevated turbulence is spread over a substantially broader area. The shear layer with (slightly) elevated turbulence between the reinjected flow and the main passage flow persists. In contrast, near the smooth endwall (Fig.3d), the peak of the TKE remains very high, but the area with high TKE level expands dramatically. The latter trend has been attributed to TLV break up, as discussed in previous papers [12,15], but it might also be associated with persistent entrainment of high PS turbulence across the tip gap. At s/c=0.55 (Fig.3e), when the blade section is located downstream of the groove, the TKE peaks in the TLV and the corner vortex decrease further, presumably since significant parts of these vortices are entrained into the groove [25] (Fig.3e). In contrast, the peak TKE and the region occupied by it still grow near the smooth endwall (Fig. 3f). In summary, when the blade passes by the groove, the TKE peaks are higher than those observed for the smooth endwall, due to the interaction of the tip flow with the groove. However, when the blade section is located downstream of the groove, entrainment of the tip flow into the groove, which also causes a lower turbulence level on the PS of the blade (owing to the reduced presence of previous TLV remnants there), reduces the turbulence level near the downstream corner of the groove.

For the high flow rate data shown in Fig.4, since data for the flow downstream of the groove is also available, we have patched the two axial views together to show a more comprehensive picture of the tip region turbulence. The resulting field of view extends from upstream of the groove (z/c_A=−0.45) to 80% of the blade chord (z/c_A=0.8). To highlight the turbulence in the shear layer extending from the upstream corner of the groove, the results are presented in insets with different scales (4:1 smaller). At s/c=0.33 (Fig.4a), the TKE peaks in the TLV and the corner vortex, as well as in the shear layer connecting the TLV to the blade, all trends appearing at low flow rates as well. The layer with elevated TKE at the interface between the main passage flow and the outflow from the groove is also evident. In addition, a broad region with elevated turbulence, which is associated with the TLV and secondary vortices generated by the previous blade, can be seen downstream of the blade PS. As discussed in [26], due to interactions of the TLV with the flow within the groove, particularly the corner vortex, the TLV lingers around the downstream corner of the groove instead of being convecting downstream by the mean flow. As a result, the elevated TKE region associated with the previous TLV is larger and located closer to the PS of the current blade at this early phase. In contrast, for the smooth endwall case (Fig.4b), the TLV just starts to roll up and detach from the blade SS corner. Hence, the associated TKE is much lower than that of the grooved.

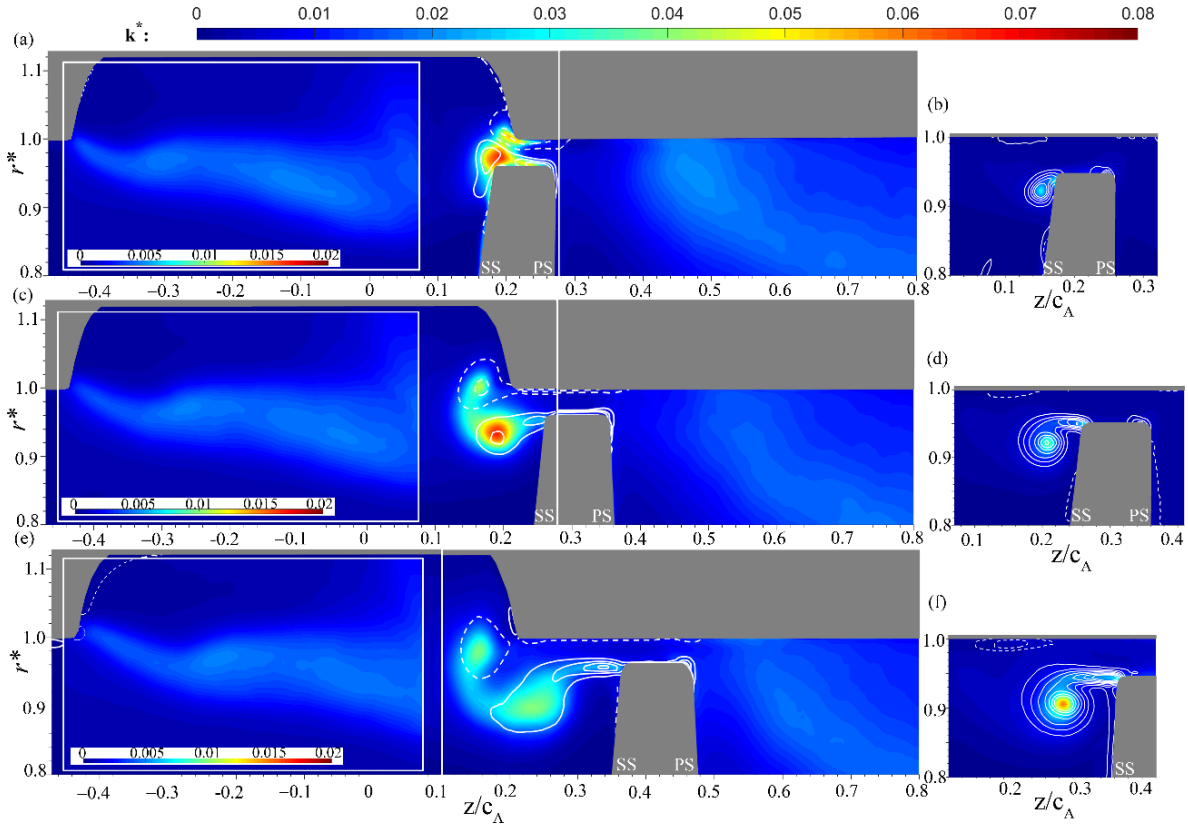

Figure 4: Evolution of turbulent kinetic energy for grooved and smooth endwalls at φ=0.35. Left column: with casing grooves; right column: smooth endwall. (a, b) s/c=0.33, (c, d) s/c=0.44, and (e, f) s/c=0.55. The insets have different color scales to highlight the elevated TKE at the upstream ends of the grooves. The vertical white line indicates matching of two sample areas.

When the blade section is already located downstream of the groove, at s/c=0.44 (Fig.4c), the TKE peak in the vortex center increases slightly, and the areas with high TKE expands. The corner vortex begins migrating towards the passage with a lower TKE peak in its center than that in the TLV. The interaction between these two vortices increases the turbulence level in the region between them as well. In addition, the blade PS is now approaching the remnant of the previous TLV, causing a slightly higher turbulence level at the PS tip corner. Compared with the smooth endwall case shown in Fig.4d, the TKE peak in the vortex center is much higher, and the associated area is much broader with a casing groove. The reason for these trends can be inferred from our previous publication [26], where we show that in instantaneous realizations, both the TLV and the corner vortex consist of multiple vortex filaments, and that interaction of the TLV with the corner vortex fragments the TLV. As discussed in an earlier work involving a different axial pump with a smooth endwall [29], interactions between the vortical filaments account for more than 40% of the TKE budget with the TLV. At a later phase (s/c=0.55), the TKE peak decreases significantly for the grooved case (Fig.4e), but the area occupied by it increases. In contrast, the peak TKE for the smooth endwall (Fig.4f) keeps on increasing, reaching a higher level than that of the grooved endwall, but the area occupied by high TKE is still concentrated around the vortex center.

The Reynolds normal stress distributions and turbulence production

This section examines and compares the distributions of normal Reynolds stress components and flow mechanisms affecting them. The phase where the blade section is located downstream of the groove (s/c=0.44) is selected as the basis for this discussion. Figure 5 compares the three Reynolds normal stresses at φ=0.25 for the smooth and grooved endwall cases. A detailed discussion of the turbulence for the smooth endwall is included in [15], so the present discussion focuses on the impact of the ACG. The first impression is the differences in magnitudes and spatial distributions of the stresses, clearly showing the anisotropy in the turbulence for both cases. Furthermore, the dominant contributors to the TKE peak in the TLV center are different. For the grooved endwall, the main contributor is the normal axial stress, $\langle u_z'u_z'\rangle$ (Fig.5a), while the radial normal stress, $\langle u_r'u_r'\rangle$, is the highest component for the smooth endwall (Fig.5d). For the grooved endwall, $\langle u_z'u_z'\rangle$ is also high in the corner vortex, and in the region located between the two vortices. Also, $\langle u_z'u_z'\rangle$ is the main contributor to the elevated turbulence in the shear layer extending from the upstream corner, and in the shear layers connecting the TLV to the blade SS corner. In contrast, for the smooth endwall (Fig.5b), $\langle u_z'u_z'\rangle$ is the primary contributor in the shear layer, but not near the TLV center. Furthermore, $\langle u_z'u_z'\rangle$ has another peak at z/c_A=0.1, i.e., upstream of the TLV, in the region where the backward tip leakage flow meets the main passage flow near the endwall.

The values of $\langle u_r'u_r'\rangle$ near the TLV center for the ACG case (Fig.5c) are much lower compared with those for the smooth

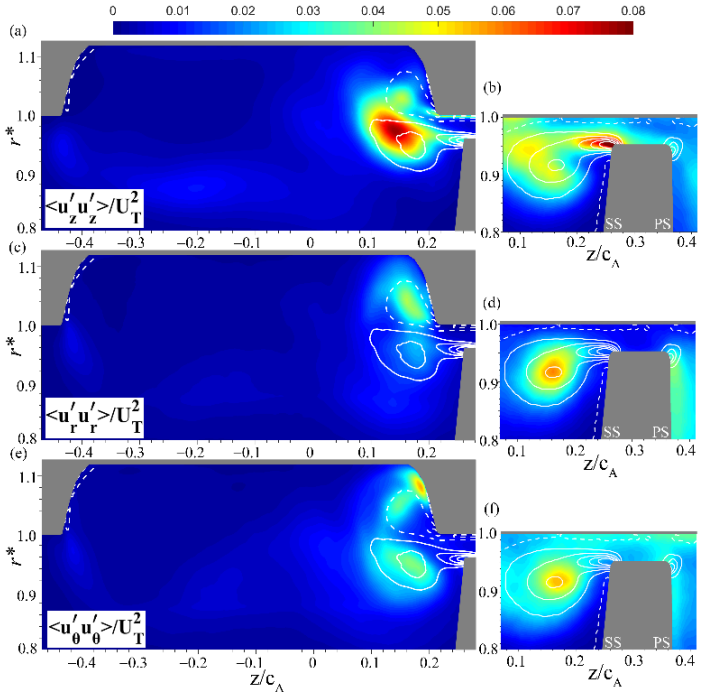

Figure 5: Distributions of normal components of the Reynolds stresses for grooved and smooth endwall cases at φ=0.25 and s/c=0.44. (a, b) $\langle u_z'u_z'\rangle/U_T^2$, (c, d) $\langle u_r'u_r'\rangle/U_T^2$, and (e, f) $\langle u_\theta'u_\theta'\rangle/U_T^2$.

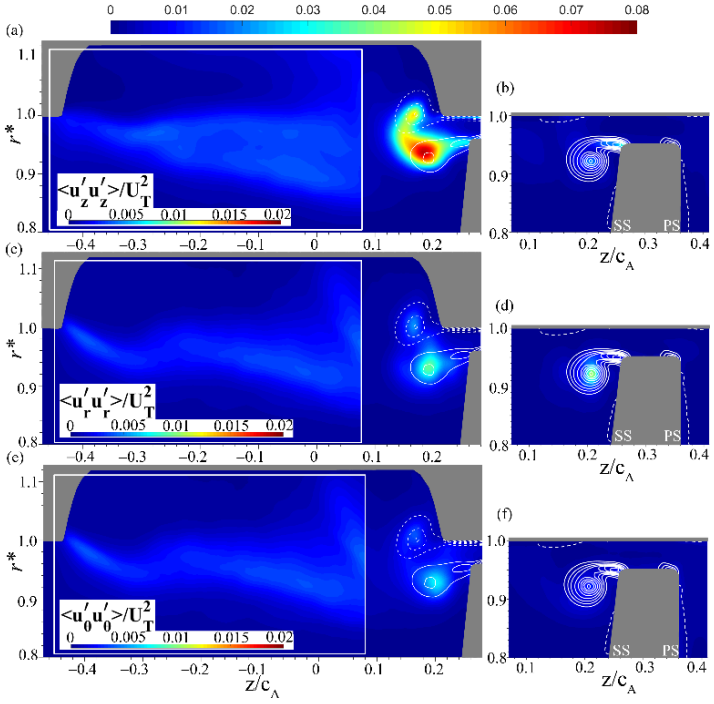

Figure 6: Distributions of normal components of the Reynolds stresses for grooved and smooth endwall cases at φ=0.35 and s/c=0.44. (a, b) $\langle u_z'u_z'\rangle/U_T^2$, (c, d) $\langle u_r'u_r'\rangle/U_T^2$, and (e, f) $\langle u_\theta'u_\theta'\rangle/U_T^2$.

endwall (Fig.5d), but they are high in the corner vortex inside the groove. As for the circumferential normal stress, $<u_\theta' u_\theta'>$ near the TLV center for the smooth endwall is higher than that of the ACG case. In a previous study, the high $<u_\theta' u_\theta'>$ near the TLV center of the smooth endwall has been attributed to circumferential contraction and associated early phases of TLV breakup [12,15]. Within the groove, $<u_\theta' u_\theta'>$ has the highest peak in the region (z/c_A=1.8, r^*=1.08) where the corner vortex interacts with the groove, indicating the flow structure inside the groove is far from being two-dimensional [25]. As discussed later, this high stress is generated by circumferential contraction when the flow decelerates circumferentially with the groove. One final note is the source for high TKE at the PS for the smooth endwall case. As Figs.5b, d&f show, all the normal stress components are elevated, but they have very different spatial distributions. The main contributors are $<u_r' u_r'>$ and $<u_\theta' u_\theta'>$ along the PS surface, but $<u_r' u_r'>$ is the main peak in the tip gap and near the endwall. As discussed later, most of the elevated turbulence along the PS is not generated locally. It is originated from the previous TLV, and is advected by the mean flow to the vicinity of the blade.

Figure 6 compares the normal Reynolds stress components for the high flow rate. Here again, the dominant term for the grooved endwall is still $<u_z' u_z'>$ (Fig.6a), and its magnitude is much higher than the corresponding values for the smooth endwall (Fig.6b). However, the confined $<u_r' u_r'>$ peak (Fig.6c) is higher than that of $<u_\theta' u_\theta'>$ (Fig.6e), and is comparable to the corresponding peak for the smooth endwall (Fig.6d). For the latter, $<u_r' u_r'>$ is still the dominant contributor to the TKE. In both cases, the values of $<u_\theta' u_\theta'>$ are lower than the other components, in contrast to the trends observed at φ=0.25 (Figs. 5e&f). Finally, within the groove, both $<u_r' u_r'>$ and $<u_\theta' u_\theta'>$ are much lower than the axial component in the corner vortex, also in contrast to the trends observed at the lower flow rate.

To explain the spatial inhomogeneity and anisotropy of the turbulence, one has to start by examining the local turbulence production rate. The TKE production rate is P=0.5(P_{zz}+P_{rr}+$P_{\theta\theta}$), where the individual terms corresponding to each of the normal stresses in the laboratory reference frame are:

$$P_{zz} = -2\left(< u'^2_z > \frac{\partial U_z}{\partial z} + < u'_r u'_z > \frac{\partial U_z}{\partial r} + < u'_\theta u'_z > \frac{1}{r}\frac{\partial U_z}{\partial \theta} \right) \quad (1)$$

$$P_{rr} = -2\left[< u'_z u'_r > \frac{\partial U_r}{\partial z} + < u'^2_r > \frac{\partial U_r}{\partial r} + < u'_\theta u'_r > \left(\frac{1}{r}\frac{\partial U_r}{\partial \theta} - \frac{U_\theta}{r} \right) - < u'_r u'_\theta > \frac{U_\theta}{r} \right] \quad (2)$$

$$P_{\theta\theta} = -2\left[< u'_z u'_\theta > \frac{\partial U_\theta}{\partial z} + < u'_r u'_\theta > \frac{\partial U_\theta}{\partial r} + < u'^2_\theta > \left(\frac{1}{r}\frac{\partial U_\theta}{\partial \theta} + \frac{U_r}{r} \right) + < u'_r u'_\theta > \frac{U_\theta}{r} \right] \quad (3)$$

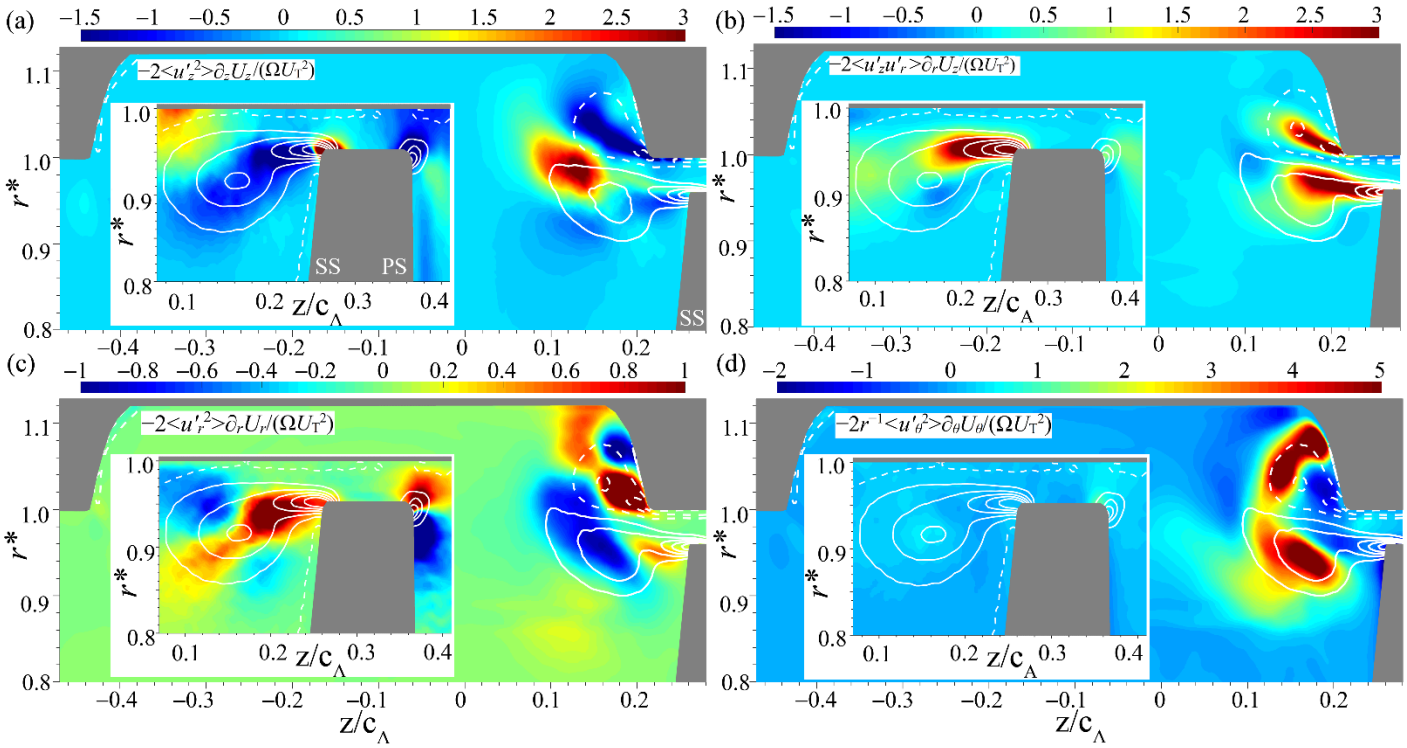

Figure 7: Distributions of dominant terms in the production rates of normal Reynolds stress components at φ=0.25 and s/c=0.44: (a)$-2<u'_z{}^2>\partial_z U_z/(\Omega U_T{}^2)$, (b) $-2<u'_z u'_r>\partial_r U_z/(\Omega U_T{}^2)$, (c) $-2<u'_r{}^2>\partial_r U_r/(\Omega U_T{}^2)$, and (d) $-2r^{-1}<u'_\theta{}^2>\partial_\theta U_\theta/(\Omega U_T{}^2)$. The insets are the smooth endwall data.

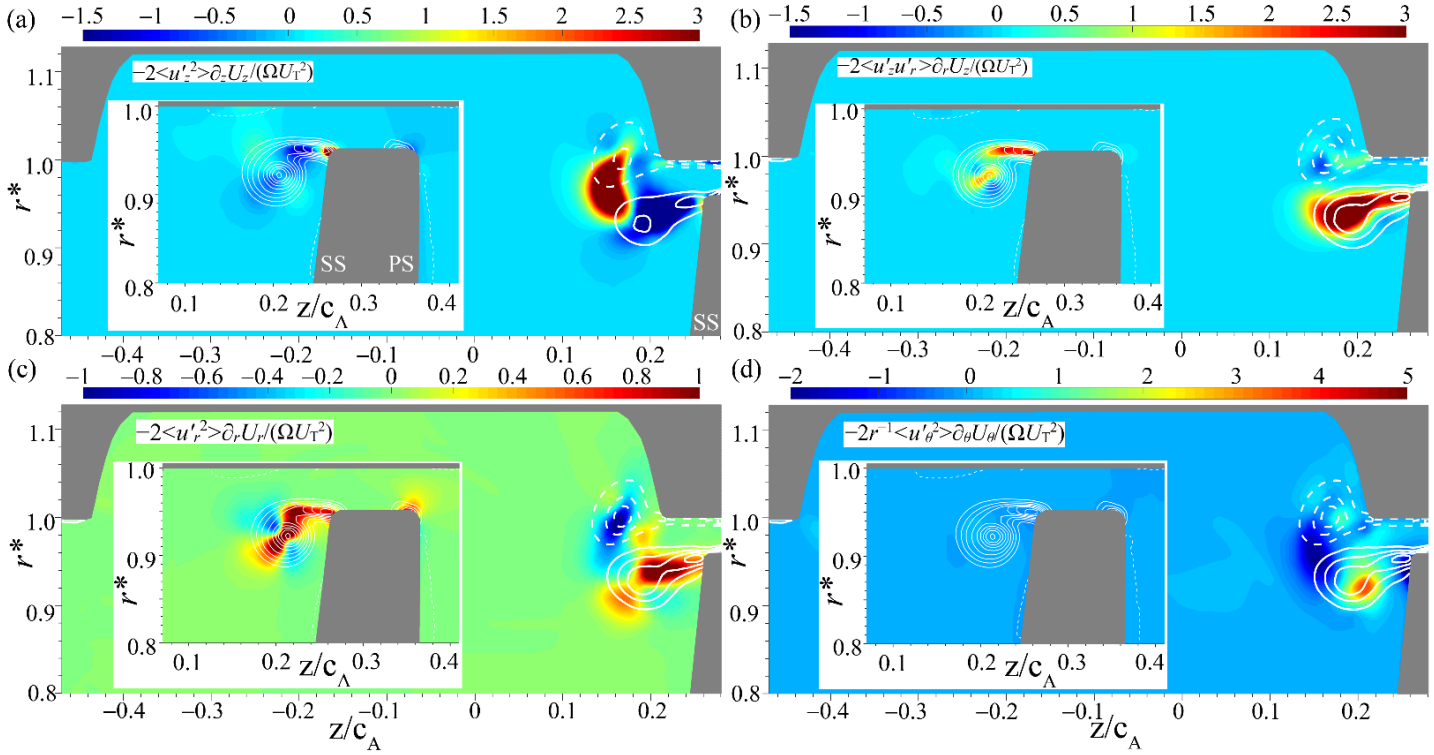

Figure 8: Distributions of dominant terms in the production rates of normal Reynolds stress components at φ=0.35 and s/c=0.44: (a) $-2\langle u'_z{}^2\rangle\partial_z U_z/(\Omega U_T{}^2)$, (b) $-2\langle u'_z u'_r\rangle\partial_r U_z/(\Omega U_T{}^2)$, (c) $-2\langle u'_r{}^2\rangle\partial_r U_r/(\Omega U_T{}^2)$, and (d) $-2r^{-1}\langle u'_\theta{}^2\rangle\partial_\theta U_\theta/(\Omega U_T{}^2)$. The insets are the smooth endwall data.

Currently, most of the terms in Eqn.1-3 can be calculated from the SPIV data, except for the terms in P_{zz} and P_{rr}, which involves $\partial U_z/\partial\theta$ or $\partial U_r/\partial\theta$. The values of $\partial U_\theta/\partial\theta$ can be obtained from the in-plane gradients using the continuity equation. In a previous study involving a smooth enwall, the out-of-plane derivatives have been measured by recording data in a series of closely-spaced meridional planes [15]. In the present analysis involving the ACGs, the discussion is restricted to the impact of available components. Some of the dominant terms in the TKE production rates are shown in Fig.7 for φ=0.25 and in Fig.8 for φ=0.35. The same terms for the smooth endwall are included as insets as a basis for comparison of trends.

Figure 7a shows the axial contraction/stretching term, namely $-2\langle u'_z{}^2\rangle\partial_z U_z/(\Omega U_T{}^2)$. Around the TLV center, this term has a diagonal four-quadrant pattern, with the sign changing from negative values where the flow is stretched axially, to positive values in regions of axial contraction. Qualitatively, this pattern is similar to that for the smooth endwall (Fig.7a insert), indicating that the flow mechanisms are similar. The particularly high production peak between the TLV and the corner vortex is the result of a strong axial contraction when the tip leakage flow is entrained into the groove, corresponding to the high $\langle u_z' u_z'\rangle$ there (Fig.5a). However, the region occupied by the corner vortex has negative values, indicating that the flow there is stretched axially. In Fig.7b, the distribution of axial shear production, $-2\langle u'_z u'_r\rangle\partial_r U_z/(\Omega U_T{}^2)$, shows that this term is high, as expected, in the shear layer connecting the TLV to the SS tip corner, and the groove corner to the corner vortex center. The effect of the latter is partially canceled by the negative production rate due to axial stretching (Fig.7a). Accordingly, the TKE peak associated within the corner vortex is significantly lower than that involving the TLV. The shear production rates in the shear layer connecting the SS corner to the TLV are high for both the smooth and grooved endwalls (Fig.7b insert).

As for the distribution of $\langle u_r' u_r'\rangle$, the trend can be explained by looking at the radial contraction/stretching production term, $-2\langle u'_r u'_r\rangle\partial_r U_r/(\Omega U_T{}^2)$, shown in Fig.7c. Entrainment of the tip leakage flow into the groove involves significant axial contraction (discussed above) and radial extension ($\partial_r U_r>0$) between the two vortices. The radial extension generates a broad area of negative production for $\langle u_r' u_r'\rangle$ staring from the TLV center to the lower part of the corner vortex. Conversely, in the corner vortex, the flow is stretched axially and contracted radially ($\partial_r U_r<0$), resulting in a high contribution to the production of $\langle u'_r u'_r\rangle$ there. These trends explain why $\langle u'_r u'_r\rangle$ is small near the TLV center but high in the corner vortex (Fig.5c). Note that the spatial distributions of $-2\langle u'_r u'_r\rangle\partial_r U_r/(\Omega U_T{}^2)$ around the TLV for the grooved and smooth (Fig.7c insert) endwalls share the inclined four quadrant pattern, but the details differ. For example, the negative regions are connected together

for the grooved endwall rather than the positive ones that are connected for the smooth endwall. Finally, the differences in the circumferential contraction/stretching production term, $-2\langle u'_\theta u'_\theta\rangle \partial_\theta U_\theta / r$ (ΩU_T^2), are striking (Fig.7d). For the grooved endwall, the circumferential production is high around the TLV and the corner vortex centers, while it is only slightly elevated for the smooth endwall. The large positive values are associated with circumferential contraction ($\partial_\theta U_\theta<0$), as the tip flow with high U_θ is slowed down at the entrance to the groove. In addition, the positive production region upstream of the TLV is associated with the circumferential velocity gradient between the flow with $U_\theta<0$ reinjected from the groove and the tip leakage flow with $U_\theta>0$. As a direct result of the elevated production due to circumferential contraction, $\langle u_\theta' u_\theta'\rangle$ is high around the TLV and the corner vortices (Fig.5e). This mechanism does not exist for the smooth endwall case.

The comparisons for φ=0.35 (Fig.8) show a few trends that are similar to those observed in Fig.7, including the four-quadrant pattern around the TLV for the axial (Fig.8a) and radial (Fig.8c) productions terms, the high shear production ($-2\langle u'_z u'_r\rangle \partial_r U_z/(\Omega U_T^2)$) in the shear layer connecting the TLV to the SS corner (Fig.8b), and the low circumferential contraction for the untreated enwall case (Fig.8d inset). However, there are several differences as well. First, the positive $-2\langle u'^2_z\rangle \partial_z U_z/(\Omega U_T^2)$ region upstream of the TLV now has a higher peak value (Fig.8a). As is evident from Fig. 2c, this strong axial contraction is associated with a rapid deceleration of the axial flow upstream of the TLV. Second, the axial shear production ($-2\langle u'_z u'_r\rangle \partial_r U_z/(\Omega U_T^2)$) in the shear layer connected to the corner vortex is low (Fig.8b), in contrast to that in Fig.7b. Third, the high circumferential contraction term ($-2r^{-1}\langle u'_\theta u'_\theta\rangle \partial_\theta U_\theta/(\Omega U_T^2)$) around the TLV and the corner vortex now disappears, with only a small peak left under the TLV. This phenomenon indicates that the circumferential deceleration of the flow exiting from the groove at high flow rate is much milder than that occurring at φ=0.25. However, this term becomes the dominant source of turbulence production again at a later phase (showing later).

Turbulence at higher chord fractions and downstream of the groove

Figure 9 examines the evolution of flow and turbulence at φ=0.35, when the blade section is located downstream of the groove. The ensemble-averaged circumferential vorticity distribution and in-plane velocity vectors are shown in the top row, followed by the TKE in the second row, and the normal Reynolds stress components in the third to fifth rows. At s/c=0.76 (Fig.9a), the TLV is much larger and has a lower peak vorticity than that at s/c=0.44 (Fig.2c). A long shear layer with high vorticity still connects the now-fragmented TLV to the blade SS tip corner. This shear layer defines the boundary between the forward passage flow and the backward tip leakage flow. The corner vortex at the groove corner is now in the process of migrating into the passage. Due to the interactions with this corner vortex, the upstream end of the TLV is latched to the groove downstream corner instead of moving downstream with the blade. These trends persist at s/c=0.87 (Fig.9b), where the peak vorticity for both vortices decreases further.

Along with the expansion of the TLV, at s/c=0.76 (Fig.9c) the area occupied by elevated TKE also expands significantly compared to that at s/c=0.55 (Fig.4e). The TKE is also broadly elevated in the corner vortex and the region of vortex interactions. In addition, The TKE is high on the PS where the remnants of a previous TLV approach the current blade. An unexpected increase in turbulence intensity occurs s/c=0.87 (Fig.9d), mostly owing to an increase in $\langle u_z' u_z'\rangle$ (compare Figs.9e&f), which is still the dominant term over a large fraction of the sample area. For both phases, the radial velocity fluctuations increase in the shear layer and under the TLV (Figs.9g&h) compared to those measured at s/c=0.44 (Fig. 6c). The circumferential fluctuations increase significantly (Figs.9i&j) in the region between the TLV and the corner vortex, making it the new dominant contributor to the TKE there. To explain some of these trends, two important production rate terms are compared in Fig.10. As is evident, the higher $\langle u_z' u_z'\rangle$ at s/c=0.87 is caused by an increase of axial shear production ($-2\langle u'_z u'_r\rangle \partial_r U_z/(\Omega U_T^2)$) shown in Figs.10a&b. This trend is associated with an increase in the Reynold shear stress $\langle u'_z u'_r\rangle$ (not shown) in the shear layer. The increase in $\langle u'_\theta u'_\theta\rangle$ is caused by particularly high production rate owing to circumferential contraction near the downstream corner of the groove. As discussed above, at this flow rate, the TLV, which has high circumferential velocity, entrains fluid with low circumferential velocity out from the groove, causing rapid deceleration of the flow in the region between the TLV and the corner vortex, near the corner of the groove. These phenomena demonstrate how interactions of the passage flow with the groove contribute directly to the expansion of the TLV and generation of high turbulence. These trends are likely contributors to the performance degradation of machine performance near the best efficiency point.

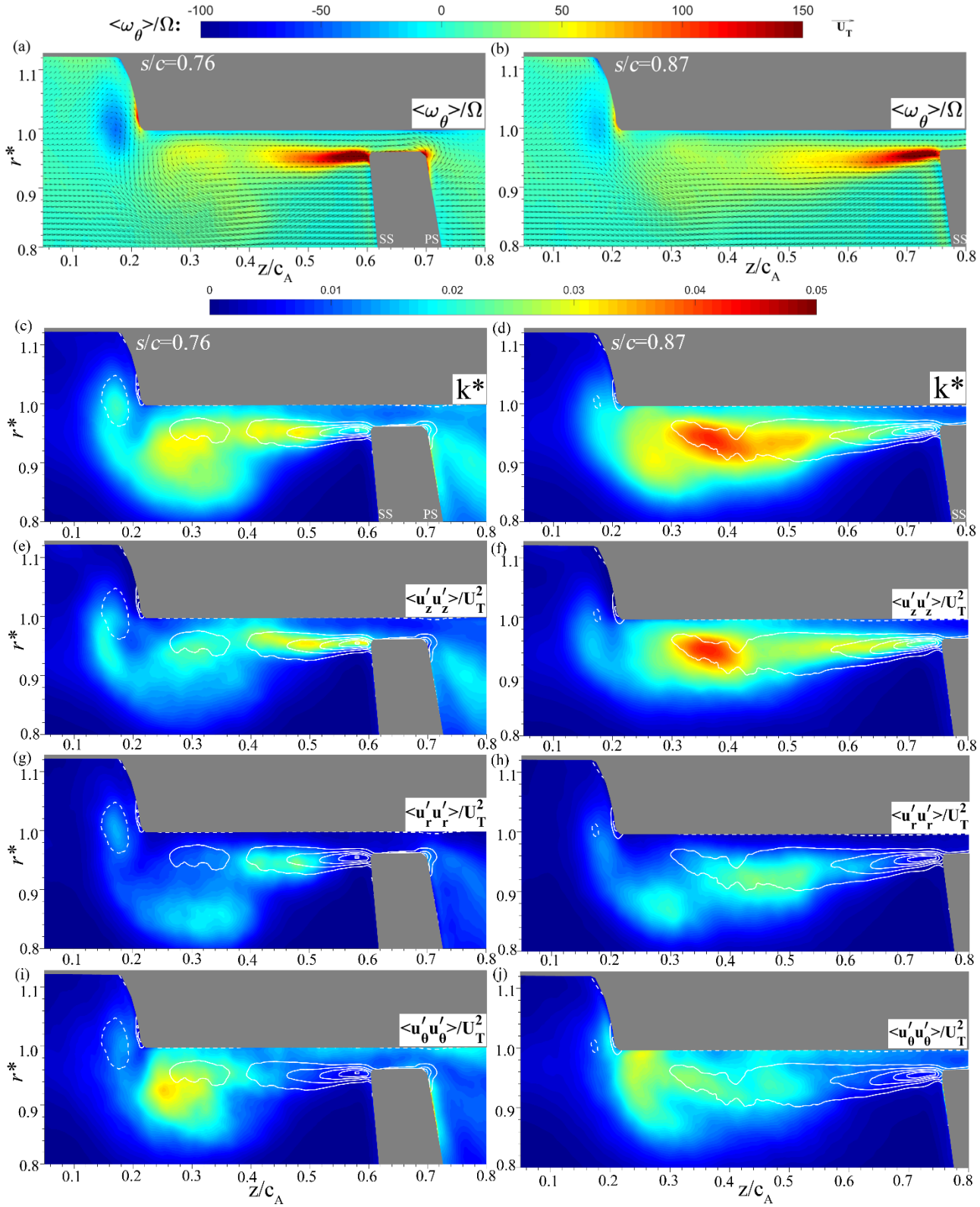

Figure 9: Evolution of the circumferential vorticity (and in-plane velocity vectors) and the tip region turbulence at φ=0.35, when the blade section is located downstream of the grooved area. Left column: s/c=0.76, and right column: s/c=0.86. (a, b) vorticity, (c, d) TKE, (e, f) $\langle u_z'u_z'\rangle/U_T^2$, (g, h) $\langle u_r'u_r'\rangle/U_T^2$ and (i, j) $\langle u_\theta'u_\theta'\rangle/U_T^2$.

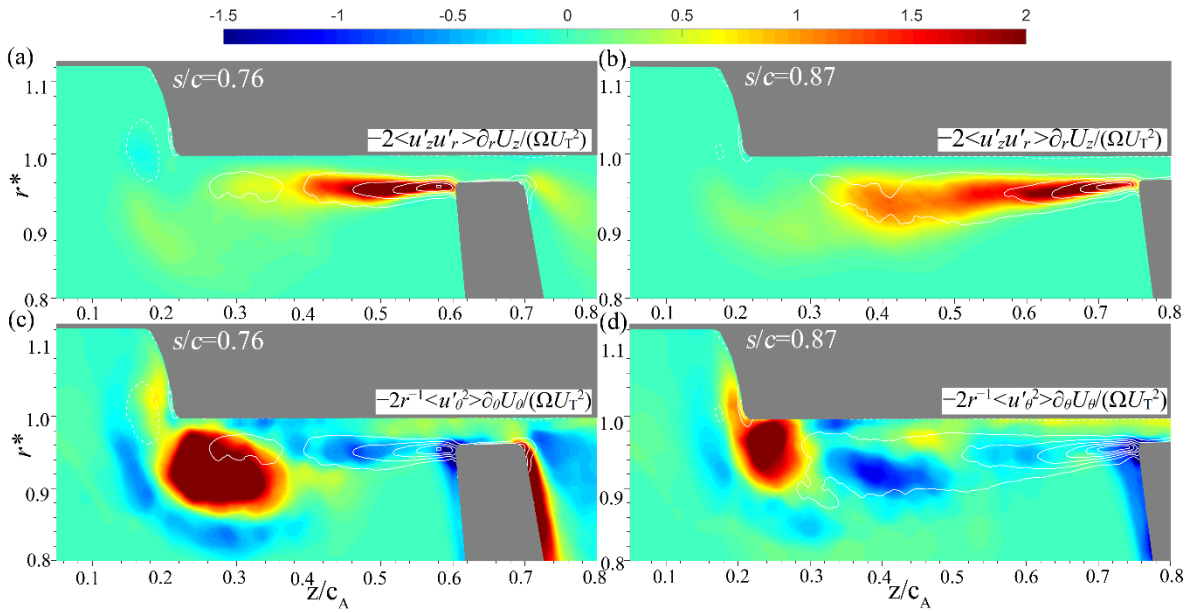

Figure 10: Dominant turbulence production terms at φ=0.35 and: (left column) s/c=0.76, and (right column) s/c=0.86. (a, b) $-2\langle u'_z u'_r\rangle \partial_r U_z/(\Omega U_T^2)$, and (c, d) $-2r^{-1}\langle u'^2_\theta\rangle \partial_\theta U_\theta/(\Omega U_T^2)$.

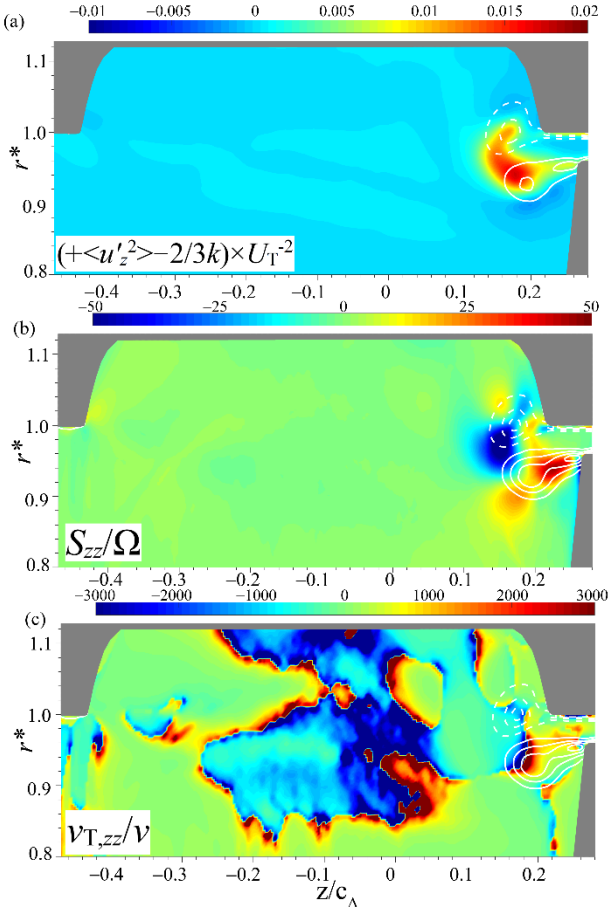

Figure 11: A sample measured distribution of eddy viscosity at s/c=0.44 and φ=0.35: (a) $(\langle u_z' u_z'\rangle - 2/3k)/U_T^2$, (b) $\partial z U z/\Omega$, and (c) the corresponding eddy viscosity normalized by the kinematic viscosity.

A brief discussion on eddy viscosity model and anisotropy

Eddy viscosity-based Reynolds stress models are still widely used as closures in applications of RANS equations. However, the above discussion shows strong anisotropy in Reynolds stresses, which challenges the fundamental assumption of these models. Our past studies [15,16] have shown large spatial variations of eddy viscosity calculated from the measured overall production rate and/or from individual Reynolds stress terms, which is caused by the non-equilibrium condition as the turbulence cannot response to the fast-changing strain fields. Figure 11 provides such a sample distribution of eddy viscosity at φ=0.35, calculated from the axial normal stress, namely $\nu_{T,zz}=(\langle u'^2_z\rangle - 2/3k)/S_{zz}$, and normalized by the kinematic viscosity of the fluid (ν). The deviatoric part of the normal stress (Fig.11a) and S_{zz} (Fig.11b) are included in the figure for comparison. The four quadrants sharped S_{zz} distribution around the tip leakage vortex is a common feature observed in our past studies [16], which affects the four quadrant pattern in turbulence production rate (Figs.7a&8a). However, a comparison between Figs.11a&b clearly shows that the Reynolds shear stress and the strain rate are spatially misaligned. As a result, the calculated $\nu_{T,zz}/\nu$ (Fig.11c) varies from negative to large positive numbers, showing no functional correlations between the stress and the strain rate. This trend applies not only to the vicinity of the TLV but also to a broad area within and below the groove, in part owing to the low stresses there. The large variations persist if the same calculations are repeated using the other stress and strain-rate components, but the values and spatial distributions vary, in agreement with previous results ([15,16]). Interestingly, as discussed in [16] and mentioned in the introduction, when trends for the same stress in different machines and operating conditions are compared, the results show spatial similarity.

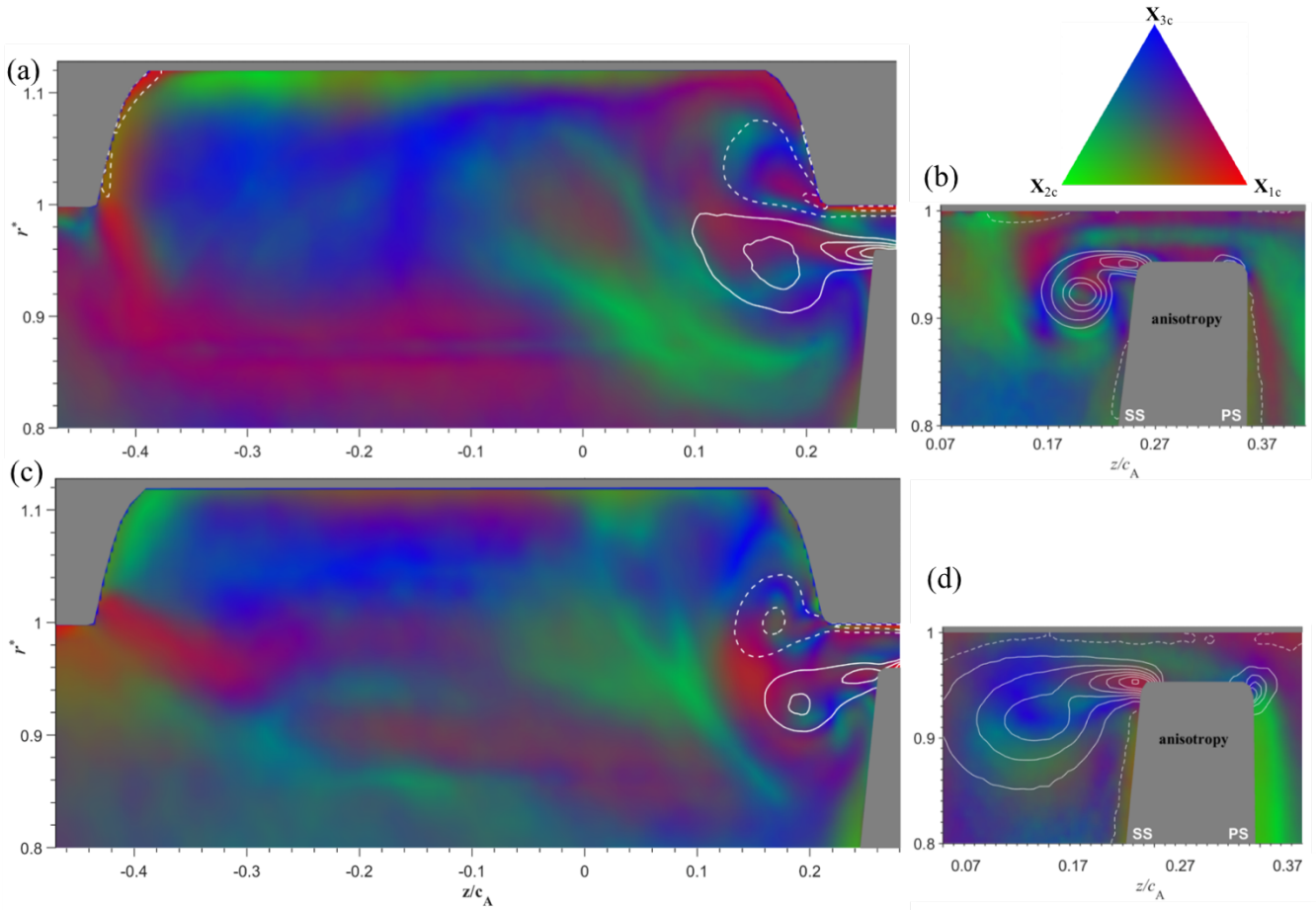

Figure 12: Anisotropy Invariant Maps (AIM) maps for: (left column) casing grooves, and (right column) smooth endwall at s/c=0.44 (a, b) φ=0.25, and (c, d) φ=0.35.

Lastly, Fig.12 shows several anisotropy invariant maps (AIM), which is a convenient means to demonstrate the spatial distribution of the anisotropy of the deviatoric part of the Reynolds stress tensor. The analysis is based on the Lumley Triangle [30,31] and involves calculations of the invariant of the anisotropy tensor ($b_{ij}=\tau_{ij}/\tau_{kk}-\delta_{ij}/3$, where τ_{ij} is the Reynolds stress tensor) at every point. The results then color-coded using RGB colors, as suggested by Emory & Iaccarino in [32]. The reference color code is provided as an equilateral triangle (shown on the top right-hand corner in Fig.12), with its three vertices representing the number of dominant components of the Reynolds stress tensor eigenvalues. The numbers one (x_{1c}, red), two (x_{2c}, green) and three (x_{3c}, blue) indicate that the local turbulence is dominated by one, two or three stress components, respectively, implying e.g., that blue regions correspond to nearly isotropic turbulence. The results show substantial spatial variations in color, but also some persistent trends among the two flow rates and/or the grooved and smooth endwalls. For example, the area occupied by the shear layer connecting the TLV to the blade SS corner is predominantly red, consistent with the previously discussed prominence of $<u_z'u_z'>$ due to the local high shear production. A large area surrounding the TLV is green for all the cases, consistent with the previously observed presence of two dominant terms, namely the radial, and circumferential stress components. In the shear layer extending from the upstream corner of the groove and separating between the outflow from the groove and the main passage flow, the color is mainly red, consistent with the dominance of $<u_z'u_z'>$. Only inside of the groove, one can observe blue regions, indicating nearly isotropic turbulence. Clearly, these AIM maps are instrumental for demonstrating and characterizing the spatial distribution of Reynolds stress anisotropy. Note, however, that they do not provide the principal directions of the eigenvectors involved. Owing to the partial similarities among the different cases suggest that such maps could be used as guidance for the development of locally tuned, data-driven turbulence models that account for the turbulence anisotropy.

CONCLUSION

The present study utilizes a large database obtained in the JHU refractive index matched facility for evaluating the effect of axial casing grooves on the evolution of turbulence in the tip region of an axial turbomachine. The distributions of turbulent kinetic energy, Reynolds normal stresses, dominant TKE and Reynolds stress production terms, as well as the anisotropy invariant maps and the eddy viscosity calculated from the

measured data are discussed and compared with those obtained for a smooth endwall in the same machine. The comparisons are performed at two flow rates, the lower one corresponding to prestall conditions in the untreated machine, and the higher one slightly below the best efficiency point. Several trends can be identified as general conclusions: (a) interactions of the tip flow and the tip leakage vortex with the groove introduce several new phenomena with elevated turbulence. The most prominent ones are the highly turbulent corner vortex and its interaction with the TLV as well as the shear layer extending from the upstream corner of the groove at the interface between the flow injected from the groove and the main passage flow. (b) Many of the observed changes to the distribution of turbulence can be explained by examining the corresponding production rate terms, in particular interactions of normal stresses with the TLV, corner vortex-induced axial contraction, and the Reynolds shear stress with regions of high shear strain rates. (c) Irrespective of flow rate and presence of grooves, the turbulence in the rotor passage and the groove is highly inhomogeneous and anisotropic, with the anisotropy invariant maps revealing spatially varying structures ranging from 1D to 2D and to 3D turbulence. While the levels of anisotropy levels vary, some common features persist, such as 1D turbulence in the shear layers, 2D turbulence in the area surrounding the TLV, and nearly isotropic turbulence within parts of the groove. (d) While presenting only one sample in the present paper for a grooved endwall, consistent with prior publications, the magnitudes, alignment and even signs of the Reynolds stresses are generally uncorrelated with the local strain-rate field. Consequently, eddy viscosity-based Reynolds stress models are unsuitable for characterizing the flow in the tip region of turbomachines. As shown in [15] for a smooth endwall, in some areas, e.g., in the shear layer connecting the TLV to the SS corner, the contribution of the turbulent stresses to the flow dynamics is comparable to that of the mean flow advection term, indicating that using the wrong turbulence model is expected to have a substantial impact on the predicted flow.

Other phenomena are flow-rate or blade phase-dependent. First, with the introduction of grooves, the dominant contributor to the TKE shifts from radial velocity fluctuations for a smooth wall to axial fluctuation for the grooved wall. This shift is predominantly (but not only) associated with increase axial contraction as the inflow or outflow from the groove interacts with the passage flow. Circumferential contraction associated with the outflux from the groove also increases the production of the circumferential velocity fluctuations is several places, including the TLV and the corner vortex at low flow rates, and around the downstream corner of the groove at high flow rates. Second, at low flow rates, the turbulence level near the groove increases substantially when the blade tip is located nearby. The TLV is partially entrained into the groove, and a corner vortex is generated owing to flow separation at the downstream corner of the groove. In contrast, at high flow rates, as the blade section shifts away from the groove, the corner vortex and flow within the groove are entrained by the TLV into the main passage, and the TLV becomes fragmented, expanding to a broad area. These processes cause an increase in shear production of axial turbulence and the above-mentioned very high circumferential contraction that increases circumferential velocity fluctuations. The latter phenomenon does not happen for a smooth endwall, and might be a contributor to the degradation of performance and the decrease in efficiency of the grooved machine at high flow rates.

ACKNOWLEDGEMENTS

This project along with the facilities and instrumentation involved have been funded in part by NASA and in part by ONR. The authors would like to thank Chunill Hah and Michael Hathaway from NASA Glenn for their guidance, and for modifying the LSAC blade geometries to match the constraints of the JHU index-matched facility. The authors would also like to express their gratitude to Yury Ronzhes who designed all the mechanical components of the test facility.

REFERENCES

[1] Lakshminarayana, B., 1986, “Turbulence Modeling for Complex Shear Flows,” AIAA J., **24**(12), pp. 1900–1917.

[2] Lakshminarayana, B., 1991, “An Assessment of Computational Fluid Dynamic Techniques in the Analysis and Design of Turbomachinery—The 1990 Freeman Scholar Lecture,” J. Fluids Eng., **113**(3), pp. 315–352.

[3] Bradshaw, P., 1996, “Turbulence Modeling with Application to Turbomachinery,” Prog. Aerosp. Sci., **32**(6), pp. 575–624.

[4] Tucker, P. G., 2013, “Trends in Turbomachinery Turbulence Treatments,” Prog. Aerosp. Sci., **63**, pp. 1–32.

[5] Moore, J. J. G., and Moore, J. J. G., 1999, “Realizability in Turbulence Modelling for Turbomachinery CFD,” *Volume 1: Aircraft Engine; Marine; Turbomachinery; Microturbines and Small Turbomachinery*, American Society of Mechanical Engineers.

[6] Durbin, P. A., 1996, “On the K-3 Stagnation Point Anomaly,” Int. J. Heat Fluid Flow, **17**(1), pp. 89–90.

[7] Lakshminarayana, B., Davino, R., and Pouagare, M., 1982, “Three-Dimensional Flow Field in the Tip Region of a Compressor Rotor Passage—Part II: Turbulence Properties,” J. Eng. Power, **104**(4), pp. 772–781.

[8] Liu, Y., Yu, X., and Liu, B., 2008, “Turbulence Models Assessment for Large-Scale Tip Vortices in an Axial Compressor Rotor,” J. Propuls. Power, **24**(1), pp. 15–25.

[9] Uzol, O., Brzozowski, D., Chow, Y.-C. C., Katz, J., and Meneveau, C., 2007, “A Database of PIV Measurements within a Turbomachinery Stage and Sample Comparisons with Unsteady RANS,” J. Turbul., **8**(August), pp. 1–20.

[10] Denton, J. D., 2010, “Some Limitations of Turbomachinery CFD,” *Volume 7: Turbomachinery, Parts A, B, and C*, ASME, pp. 735–745.

[11] Horlock, J. H., and Denton, J. D., 2005, “A Review of

Some Early Design Practice Using Computational Fluid Dynamics and a Current Perspective," J. Turbomach., **127**(1), pp. 5–13.

[12] Wu, H., Tan, D., Miorini, R. L., and Katz, J., 2011, "Three-Dimensional Flow Structures and Associated Turbulence in the Tip Region of a Waterjet Pump Rotor Blade," Exp. Fluids, **51**(6), pp. 1721–1737.

[13] Wu, H., Miorini, R. L., and Katz, J., 2010, "Analysis of Turbulence in the Tip Region of a Waterjet Pump Rotor," *ASME 2010 3rd Joint US-European Fluids Engineering Summer Meeting: Volume 1, Symposia – Parts A, B, and C*, ASME, pp. 699–711.

[14] Li, Y., Chen, H., Tan, D., and Katz, J., 2019, "On the Effects of Tip Clearance and Operating Condition on the Flow Structures Within an Axial Turbomachine Rotor Passage," J. Turbomach., **141**(11).

[15] Li, Y., Chen, H., and Katz, J., 2017, "Measurements and Characterization of Turbulence in the Tip Region of an Axial Compressor Rotor," J. Turbomach., **139**(12), p. 121003.

[16] Li, Y., Chen, H., and Katz, J., 2019, "Challenges in Modeling of Turbulence in the Tip Region of Axial Turbomachines," J. Sh. Res., pp. 1–13.

[17] Moore, R. D., Kovich, G., and Blade, R. J., 1971, "Effect of Casing Treatment on Overall and Blade Element Performance of a Compressor Rotor," NASA Techincal Note, p. TN D-6538.

[18] Osborn, W. M., Lewis, G. W. J., and Heidelberg, L. J., 1971, "Effect of Several Porous Casing Treatments on Stall Limit and on Overall Performance of an Axial-Flow Compressor Rotor," NASA Techincal Note, p. TN D-6537.

[19] Takata, H., and Tsukuda, Y., 1977, "Stall Margin Improvement by Casing Treatment --- Its Mechanism and Effectiveness," J. Eng. Power, **99**(1), pp. 121–133.

[20] Smith, G. D. J., and Cumpsty, N. A., 1984, "Flow Phenomena in Compressor Casing Treatment," J. Eng. Gas Turbines Power, **106**(3), pp. 532–541.

[21] Brandstetter, C., Kegalj, M., Wartzek, F., Heinichen, F., and Schiffer, H.-P., 2014, "Stereo PIV Measurement of Flow Structures underneath an Axial-Slot Casing Treatment on a One and a Half Stage Transonic Compressor," *17th International Symposium on Applications of Laser Techniques to Fluid Mechanics*, Lisbon, Portugal, pp. 1–18.

[22] Crook, A. J., Greitzer, E. M., Tan, C. S., and Adamczyk, J. J., 1993, "Numerical Simulation of Compressor Endwall and Casing Treatment Flow Phenomena," J. Turbomach., **115**(3), pp. 501–512.

[23] Fujita, H., and Takata, H., 1984, "A Study on Configurations of Casing Treatment for Axial Flow Compressors," Bull. JSME, **27**(230), pp. 1675–1681.

[24] Müller, M. W., Schiffer, H.-P., Voges, M., and Hah, C., 2011, "Investigation of Passage Flow Features in a Transonic Compressor Rotor," *Proceedings of ASME Turbo Expo 2011: Power for Land, Sea and Air*, Vancouver, Canada, pp. 1–11.

[25] Chen, H., Li, Y., Koley, S. S., Doeller, N., and Katz, J., 2017, "An Experimental Study of Stall Suppression and Associated Changes to the Flow Structures in the Tip Region of an Axial Low Speed Fan Rotor by Axial Casing Grooves," J. Turbomach., **139**(12), p. 121010.

[26] Chen, H., Li, Y., and Katz, J., 2019, "On the Interactions of a Rotor Blade Tip Flow With Axial Casing Grooves in an Axial Compressor Near the Best Efficiency Point," J. Turbomach., **141**(1), p. 011008.

[27] Tan, D., Li, Y., Wilkes, I., Miorini, R. L., and Katz, J., 2015, "Visualization and Time-Resolved Particle Image Velocimetry Measurements of the Flow in the Tip Region of a Subsonic Compressor Rotor," J. Turbomach., **137**(4), p. 041007.

[28] Chen, H., Li, Y., Tan, D., and Katz, J., 2017, "Visualizations of Flow Structures in the Rotor Passage of an Axial Compressor at the Onset of Stall," J. Turbomach., **139**(4), p. 041008.

[29] Miorini, R. L., Wu, H., and Katz, J., 2012, "The Internal Structure of the Tip Leakage Vortex Within the Rotor of an Axial Waterjet Pump," J. Turbomach., **134**(3), p. 031018.

[30] Lumley, J. L., 1979, "Computational Modeling of Turbulent Flows," *Advances in Applied Mechanics*, pp. 123–176.

[31] Simonsen, A. J., and Krogstad, P.-Å., 2005, "Turbulent Stress Invariant Analysis: Clarification of Existing Terminology," Phys. Fluids, **17**(8), p. 088103.

[32] Emory, M., and Iaccarino, G., 2014, "Visualizing Turbulence Anisotropy in the Spatial Domain with Componentality Contours," Cent. Turbul. Res. Annu. Res. Briefs, pp. 123–138.